The Meteoritical Society

Meteoritics & Planetary Science 53, Nr 9, 1805–1819 (2018)
doi: 10.1111/maps.13124

Compositional variability on the surface of 1 Ceres revealed through GRaND measurements of high-energy gamma rays

David J. LAWRENCE[1*], Patrick N. PEPLOWSKI[1], Andrew W. BECK[1], William C. FELDMAN[2], Thomas H. PRETTYMAN[2], Chris T. RUSSELL[3], Michael J. TOPLIS[4], Jack T. WILSON[1], Eleonora AMMANNITO[5,6], Julie C. CASTILLO-ROGEZ[7], M. C. DESANCTIS[6], Scott C. MEST[2], and Adrian NEESEMANN[8]

[1]Johns Hopkins University Applied Physics Laboratory, Laurel, Maryland 20723, USA
[2]Planetary Science Institute, Tucson, Arizona 85719, USA
[3]University of California Los Angeles, Los Angeles, California 90095, USA
[4]L'Institut de Recherche en Astrophysique et Planétologie, Toulouse, France
[5]Agenzia Spaziale Italiana, Roma, Italy
[6]Istituto di Astrofisica e Planetologia Spaziali, Istituto Nazionale di Astrofisica, Roma, Italy
[7]Jet Propulsion Laboratory, Pasadena, California 91109, USA
[8]Institute of Geological Sciences, Freie Universität Berlin, Berlin, Germany
[*]Corresponding author. E-mail: david.j.lawrence@jhuapl.edu

(Received 01 December 2017; revision accepted 08 May 2018)

Abstract–High-energy gamma rays (HEGRs) from Ceres's surface were measured using Dawn's Gamma Ray and Neutron Detector (GRaND). Models of cosmic-ray-initiated gamma ray production predict that the HEGR flux will inversely vary with single-layer hydrogen concentrations for Ceres-like compositions. The measured data confirm this prediction. The hydrogen-induced variations in HEGR rates were decoupled from the measurements by detrending the HEGR data with Ceres single-layer hydrogen concentrations determined by GRaND neutron measurements. Models indicate that hydrogen-detrended HEGR counting rates correlate with water-free average atomic mass, which is denoted as <A>*. HEGR variations across Ceres's surface are consistent with <A>* variations of ±0.5 atomic mass units. Chemical variations in the CM and CI chondrites, our closest analogs to Ceres's surface, suggest that <A>* variations on Ceres are primarily driven by variations in the concentration of Fe, although other elements such as Mg and S could contribute. Dawn observations have shown that Ceres's interior structure and surface composition have been modified by some combination of physical (i.e., ice-rock fractionation) and/or chemical (i.e., alteration) processes that has led to variations in bulk surface chemistry. Locations of the highest inferred <A>* values, and thus possibly the highest Fe and least altered materials, tend to be younger, less cratered surfaces that are broadly associated with the impact ejecta of Ceres's largest craters.

INTRODUCTION

The Dawn spacecraft has been investigating the dwarf planet Ceres since its arrival in March 2015 (Russell et al. 2016). One of the major objectives of the Ceres portion of the Dawn mission is to measure and characterize mineralogical and elemental composition of Ceres's surface. Elemental composition data are obtained with Dawn's Gamma Ray and Neutron Detector (GRaND), which has shown that Ceres has large hydrogen abundances in the range of 16–29 wt% water equivalent hydrogen (WEH) (Prettyman et al. 2017). The spatial variation of WEH abundances shows strong latitude dependence, with the largest values at the north and south poles. The measured hydrogen shows evidence for significant depth variation, where the high abundances near the poles are likely stable at or near the surface, but for more equatorial regions, the high abundances are

located tens of centimeters to meters below the surface (Prettyman et al. 2017). Analyses of GRaND data show that the concentration of Fe is lower than typical chondritic values for regions where ice is deeper than can be sensed by GRaND. This suggests that Ceres could have experienced ice-rock fractionation or dilution by a neutral component such as C, resulting in differences between Ceres's surface and bulk composition (Prettyman et al. 2017). Spectral reflectance data from Dawn's Visible and Infrared Mapping Spectrometer (VIR) show that Ceres's surface contains abundant NH_4- and Mg-bearing phyllosilicates and carbonates (De Sanctis et al. 2015, 2016), where the concentrations of these materials vary across the surface (Ammannito et al. 2016). In addition, localized water-ice signatures have been detected with VIR data (Combe et al. 2016). Taken together, these observations reveal a world that is rich in water and water-bearing species, and where aqueous alteration processes played an important role in shaping the surface and its interior.

We report surface composition information derived from GRaND-measured high-energy gamma rays (HEGR). While not yet a standard product of planetary nuclear spectroscopy instruments, HEGRs provide useful composition information that is complementary to element-specific gamma ray measurements and neutron composition parameters. Specifically, HEGRs provide a measure of average elemental composition related to average atomic mass (<A>), and when combined with other elemental composition information, HEGRs can provide unique elemental abundance maps (Peplowski and Lawrence 2013; Peplowski et al. 2013). At Vesta, HEGRs were used to map variations in the igneous origins of surface materials. At Ceres, we find that HEGRs provide hydrogen composition information complementary to that inferred from GRaND neutron data, as well as new information about nonhydrogen elemental compositions.

In this paper, we provide a brief summary of HEGRs and their use for planetary composition measurements. Next, we present modeling results of HEGRs for a water-rich body, and then apply these results to HEGR measurements of Ceres. Finally, we discuss the GRaND-measured HEGR data and compare these data with other Dawn measurements at Ceres and summarize the overall results.

PLANETARY HIGH-ENERGY GAMMA RAYS: BACKGROUND

Planetary gamma ray spectroscopy is a technique that derives planetary elemental compositions from measurements of galactic cosmic-ray (GCR)-generated gamma rays (Prettyman 2014). Gamma ray spectroscopy typically uses single gamma ray lines located at element-characteristic energies to report the elemental composition of the given elements. In contrast, HEGRs are defined as broad-band emission in the energy range of 8 to ~9 MeV. It was recognized by Peplowski and Lawrence (2013) that HEGRs can provide composition information that is independent of standard line-emission gamma rays. Specifically, HEGRs are produced primarily by the decay of GCR-generated pions within planetary materials. Based on both theoretical considerations and experimental evidence, Peplowski and Lawrence (2013) showed that HEGRs have a compositional dependence that roughly scales as average atomic mass, <A>. HEGRs can therefore be used in a similar way as neutron composition parameters that measure neutron absorption, moderation, and <A> with GCR-generated thermal, epithermal, and fast neutrons, respectively (e.g., Feldman et al. 2011; Maurice et al. 2011; Lawrence et al. 2013; Prettyman et al. 2013). The study of Peplowski and Lawrence (2013) worked out a systematic understanding of HEGRs using data from the Moon acquired with the Lunar Prospector Gamma-Ray Spectrometer (LP-GRS). The dominant elemental variabilities of HEGRs in lunar materials are Fe, Ti, and Mg. Since Fe and Ti have been independently measured at the Moon (e.g., Prettyman et al. 2006), the HEGR variations from these elements were removed and Peplowski and Lawrence (2013) reported an inferred map of lunar Mg abundances.

In addition to the lunar measurements, HEGR composition information was reported from the asteroid 4 Vesta based on GRaND data (Peplowski et al. 2013). That work showed spatial variations in HEGR count rates that generally corresponded to known variations in igneous rock type. A combination of radiation transport modeling and constraints from the Vesta-originating howardite, eucrite, and diogenite (HED) meteorites were used to relate HEGR count rates to plutonic (digenitic) and basaltic (eucritic) rock types. These data provided independent composition information that was subsequently combined with other neutron and gamma-ray compositional data to refine our understanding of Vesta's chemical composition (Beck et al. 2015), and that ultimately led to the identification of a compositional terrain near Vesta's north pole (Beck et al. 2017) that is underrepresented in the HED meteorite collection.

The goal of this study was to build upon the lunar and vestan HEGR studies to understand what information HEGRs can provide about Ceres. The main difference between this study and the prior measurements is that Ceres has relatively large amounts of water (or WEH) compared to the Moon and Vesta, which have hydrogen concentrations of hundreds of ppm or less (Prettyman et al. 2012; Lawrence et al. 2015). In the initial study of HEGRs, Peplowski and Lawrence (2013) mentioned that HEGR systematic variations with hydrogen had not been

studied. The GRaND Ceres data therefore provide a good opportunity to understand how HEGRs vary with hydrogen as well as other elements.

HEGR MODELS FOR WATER-RICH COMPOSITIONS AT CERES

Peplowski and Lawrence (2013) defined a HEGR composition parameter, C_p, and showed that to a good approximation, C_p is proportional to the total cross section, σ_T for pion production, where

$$\sigma_T = \sum_i f_i \sigma_i, \quad (1)$$

and

$$\sigma_i = \frac{3}{2}\left[24.5 Z_i^{\frac{1}{3}} + 2.33 N_i^{\frac{2}{3}}\right]. \quad (2)$$

Here, Z_i and N_i are the atomic and neutron numbers, respectively, for each element i within each material type. f_i in Equation 1 is the molar fraction for each element, and the summation is over all elements in the material. As noted by Peplowski and Lawrence (2013), the scaling relationships in Equation 2 do not hold for light elements ($Z \leq 6$) such that for hydrogen and carbon, the $Z^{1/3}$ coefficient is closer to 10 and the $N^{2/3}$ coefficient is closer to 1 (i.e., pion production decreases for the light elements) (Cochran et al. 1972). Nevertheless, even with this complication, Equations 1 and 2 suggest that the HEGR flux should decrease as the hydrogen content increases.

To understand how HEGRs vary for Ceres-like compositions, we modeled HEGR fluxes using the particle transport code MCNPX (Pelowitz 2005), a code that has been used to derive gamma-ray and neutron fluxes for other studies of various planetary bodies (e.g., Prettyman et al. 2006; Lawrence et al. 2013; Peplowski et al. 2015). Ceres compositions are simulated using the same five material types that were used by Prettyman et al. (2017). These materials are "CI" and "CM," which represent average CI and CM chondrite meteorite abundances, and "E1," "E2," and "E3," which are materials that have progressively lower Fe and higher C and S abundances than the meteorite analogs. A primary focus of these simulations is to understand the variation of HEGRs with hydrogen. In addition, because the five materials used here have a range of nonhydrogen <A> values (see below), <A> variations will also be investigated with the results of these simulations. For each of these material compositions, water was added with concentrations ranging from 15 wt% to 55 wt%, a variation that encompasses the measured values at Ceres, which range from 16 wt% to 29 wt% (Prettyman et al. 2017).

The variation of simulated HEGR fluxes versus WEH and <A> is shown in Fig. 1. The HEGR fluxes have a clear inverse correlation with WEH abundances (Fig. 1a) as suggested by Equations 1 and 2. In addition, each material shows parallel trend lines that suggest there is an additional compositional dependence within the simulated HEGR flux that is beyond the WEH variation. Within each material, the simulated HEGR flux varies by 22% from minimum to maximum. For the same material compositions, the parameterized pion production cross section of Equation 2 varies by 29% from minimum to maximum (using the smaller $Z^{1/3}$ and $N^{2/3}$ coefficients for hydrogen and carbon as given by Cochran et al. [1972]). This general agreement between the magnitude of variation for HEGR production and pion cross sections further supports the hypothesis of Peplowski and Lawrence (2013) that the HEGR compositional variability is mostly driven by the composition-dependent variations of pion production as expressed in Equations 1 and 2. The HEGR flux is positively correlated with <A> (Fig. 1b), and as with the WEH dependence, each material follows a parallel trend line.

For this set of compositions with artificially varying WEH abundances, the values of WEH and <A> are not independent of each other. Rather, most of the HEGR variation with <A> is merely a consequence of the primary HEGR variation with hydrogen. This WEH and <A> dependence can be decoupled by defining a water-free average atomic mass, <A>* as:

$$\frac{1}{\langle A \rangle^*} = \sum_{i \neq H_2O} \frac{w_i}{A_i}, \quad (3)$$

where the summation of the ratio of weight fraction w_i and atomic mass A_i for each element i is calculated over all elements except the hydrogen and oxygen from the water fraction. With this definition, the five materials now have only five <A>* values ranging from material "E3," which has the smallest <A>* value, to CM, which has the largest. The variation of modeled HEGR production versus <A>* is shown in Fig. 2a, where the separate variations due to WEH and <A>* are clearly apparent. Each parallel trend line represents a distinct WEH value with the largest WEH values having the lowest HEGR fluxes. This WEH dependence can be removed by detrending the simulated relationship between HEGR flux and WEH, which is represented by the dashed line in Fig. 1a. With this detrended dependence (Fig. 2b), the HEGR variation is significantly reduced, and the remaining HEGR variation is dominantly due to variations in <A>*. This procedure shows that for the simulated HEGR fluxes, the WEH dependence can be successfully decoupled from the water-free average

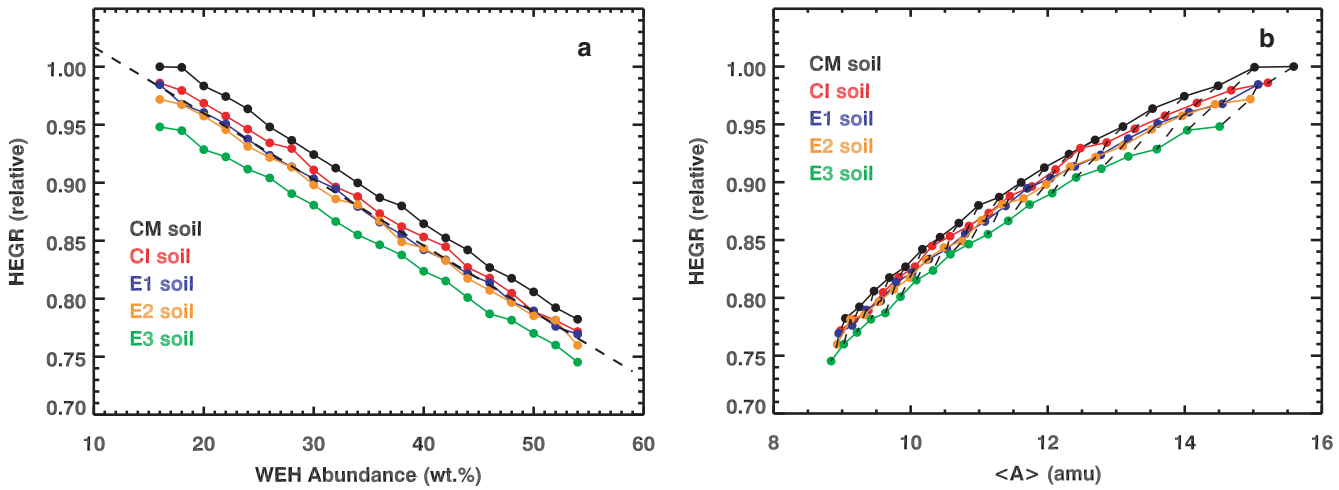

Fig. 1. Simulated high-energy gamma ray (HEGR) flux for three different soil compositions given by Prettyman et al. (2017). For each of these compositions, the water equivalent hydrogen (WEH) abundances were varied from 15 wt% to 55 wt%. The values are given relative to the highest value in the group, which is the CM soil at 15 wt%. The relative one-sigma statistical uncertainties from the Monte Carlo calculation are 0.3%, which is roughly the size of the plotting symbols. a) HEGR flux versus WEH abundance. Dashed line shows the average HEGR versus WEH trend line. b) HEGR flux versus soil average atomic mass <A> in units of atomic mass units (amu). (Color figure can be viewed at wileyonlinelibrary.com.)

atomic mass dependence. Thus, when analyzing the GRaND data, we expect to be able to carry out a similar procedure.

HEGR DATA FROM CERES

The HEGR data from GRaND were processed in a manner similar to prior analyses (e.g., Lawrence et al. 2013; Peplowski et al. 2013), as well as the recent analysis of GRaND Ceres data (Prettyman et al. 2017). This processing includes data selections for good viewing geometry and valid data. Corrections were made to the data to minimize noncompositional variations from GCRs and solid-angle changes. Prior to creating final maps, we carried out a smoothing algorithm to maximize the signal-to-background in the mapped data. A summary of the specific processing steps is given in the Appendix.

The data used in this analysis include data taken from various portions of GRaND orbit phases around Ceres (Prettyman 2016; Prettyman and Yamashita 2016). The primary Ceres gamma-ray data were taken from the Dawn Low-Altitude Mapping Orbit (LAMO) and extended LAMO phase, for dates ranging from December 16, 2015 to August 10, 2016. The end of the data accumulation period for this study, which precedes the end of the extended LAMO phase, was chosen to avoid sensor gain changes that were made to GRaND after August 10, 2016. High-altitude data from before and after the LAMO phases were also used for background determination. Pre-LAMO background data were used from March 16, 2015 to July, 2015. Post-LAMO background values used data from January 29, 2017 to July 7, 2017. Figure 3 shows the average gamma-ray spectrum for all LAMO and background orbit phases. The energy boundaries for the HEGRs were chosen to be 8–8.6 MeV, in comparison to the 8–8.7 MeV for the GRaND Vesta study of Peplowski et al. (2013). These values were selected to avoid overlap with the 7.6-MeV Fe gamma ray doublet, as well as the high-energy limit resulting from the signal processing chain (the high-energy discriminator).

A map of the HEGR count rate variation (relative to the mean value) is shown in Fig. 4. By inspection, this map clearly has an inverse relationship to the map of Ceres hydrogen concentrations (Prettyman et al. 2017), which has higher hydrogen concentrations in the polar regions and lower hydrogen concentrations in the equatorial regions. This result thus confirms the model prediction that the HEGRs should be inversely related to hydrogen concentrations. The minimum and maximum relative HEGR values are 0.95 and 1.05, respectively, for a dynamic range of 10%. Using the model HEGR-versus-hydrogen-abundance variation of 0.0057-HEGR-relative-counts-per WEH wt% (the average line slope of Fig. 1a), the full measured HEGR variation corresponds to a model-based hydrogen variation of 17.5 wt% WEH, which is larger than the neutron-measured variation of 13 wt% WEH (=29–16 wt% WEH). However, when using the data-based slope value of 0.0067 (see Fig. 5), the implied WEH dynamic range is 15 wt%, which is closer to the measured neutron-based value.

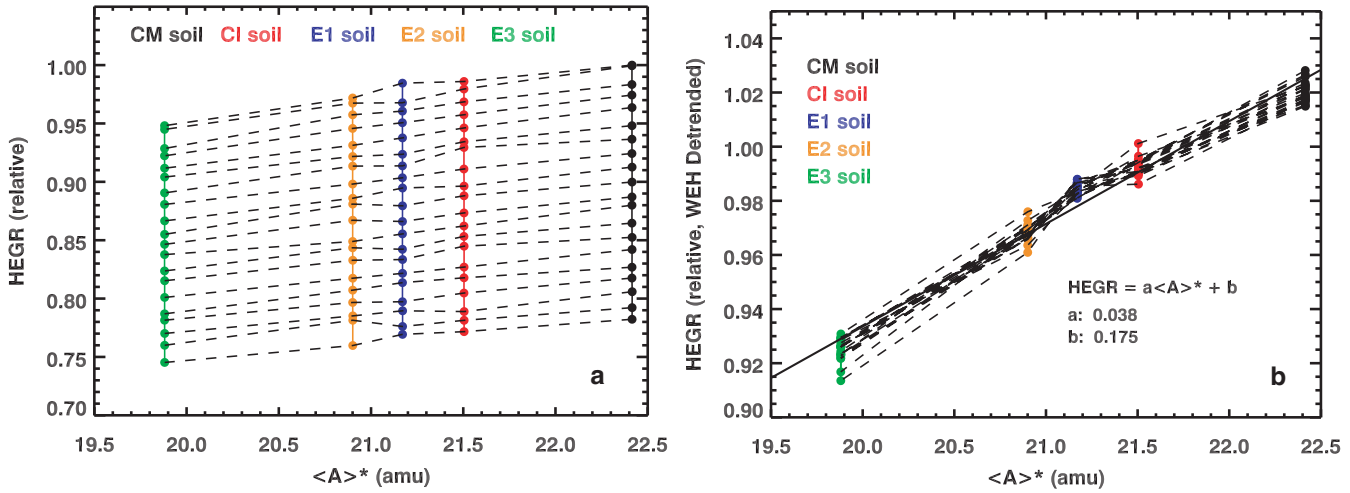

Fig. 2. a) Relative HEGR flux values given in Fig. 1, but now plotted versus water-free average atomic mass <A>*. b) HEGR fluxes, which have been detrended using the dashed line from Fig. 1a, plotted versus <A>*. The detrending procedure is mathematically the same as used later in Equation 4 and Fig. 5 for the Ceres data. For each soil trend, an offset value has been added that is equivalent to the original value at 15 wt% WEH. (Color figure can be viewed at wileyonlinelibrary.com.)

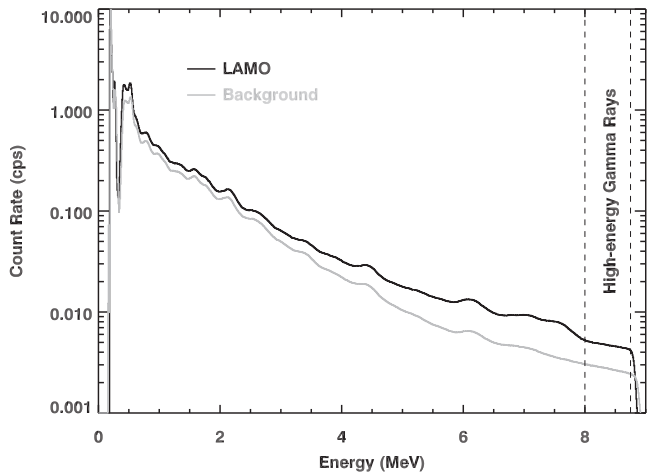

Fig. 3. GRaND gamma-ray spectra measured from the LAMO mission phase (black) and high-altitude background mission phases (gray) as described in the text. Vertical dashed lines show the energy boundaries for the HEGRs used in this study.

The quantitative relationship between measured HEGRs and hydrogen abundance is shown as a scatter plot in Fig. 5. The expected anticorrelation between the two measurements is clearly seen, but with some deviations from a linear trend. To isolate what appears to be the linear portion of the HEGR-versus-hydrogen variation, a linear fit was applied to the fifth-percentile values in the linear range (19–26 wt% WEH) of the data in Fig. 5. The slope of the measured trend (0.0067 relative-counts-per WEH wt%) is within 15% of the model-based trend. The hydrogen-varying portion of the HEGR data was then decoupled by detrending the linear relationship using:

$$C_{\mathrm{HEGR,\ No\ WEH}} = C_{\mathrm{HEGR}} - (a[WEH] + b), \qquad (4)$$

where C_{HEGR} is the original HEGR count rate, a and b are the linear fit parameters, $[WEH]$ is WEH wt%, and $C_{\mathrm{HEGR,\ No\ WEH}}$ is the detrended HEGR count rate. Since this is the same procedure used for decoupling the model HEGR count rates, we propose that the detrended measured count rates are proportional to Ceres's hydrogen-free average atomic mass, <A>*. A map of the WEH-detrended HEGR count rates is shown in Fig. 6. As one measure of possible systematic uncertainties, a detrending analysis was carried out for the full range of WEH concentrations and 50th-percentile binned values. In this case, the slope was 7% higher than with the fifth-percentile values, and the detrended map varied by <1% from the map shown in Fig. 6. A discussion of how the WEH-detrended map relates to our knowledge of Ceres-like compositions is described in the next section, and how it relates to other Dawn Ceres measurements is given in the section following.

DISCUSSION OF WEH-DETRENDED HEGR MAP

As mentioned above, the model results, coupled with the model-predicted HEGR anticorrelation with WEH, strongly suggest that the WEH-detrended HEGR map is proportional to Ceres's hydrogen-free average atomic mass <A>*. In this section, we discuss the broad implications of this idea. First, we note that the detrended HEGR values have a 3.7% dynamic range across Ceres's surface. Vesta and the Moon, the only

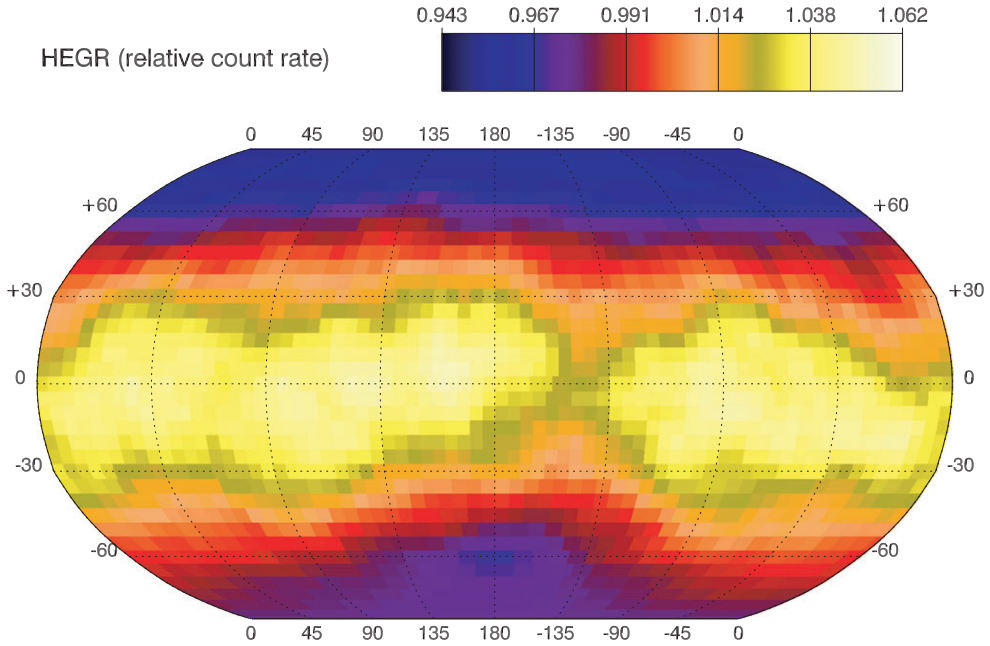

Fig. 4. Map of HEGR count rates relative to the mean. (Color figure can be viewed at wileyonlinelibrary.com.)

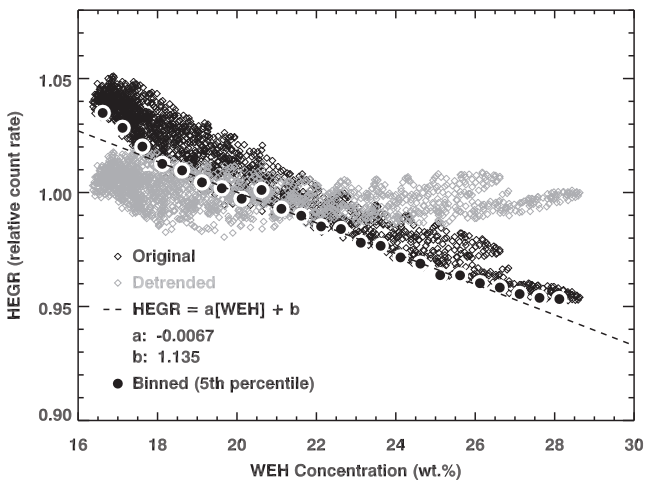

Fig. 5. HEGR count rates versus WEH concentrations as given by Prettyman et al. (2017). The original HEGR data are shown as black diamonds. Black circles show fifth-percentile HEGR values in WEH bins. The dashed line shows a linear fit of the binned values for linear portion of the binned data points that range from 19 to 26 wt%. The fit parameters for this line are shown. The gray diamonds show HEGR values that have been detrended using the dashed line.

other bodies for which HEGR analyses have been performed, have dynamic ranges of 5% and 18%, respectively (Peplowski and Lawrence 2013; Peplowski et al. 2013). Thus, of the three reported measurements, Ceres has the smallest hydrogen-free HEGR dynamic range and is close to the 3% dynamic range seen with fast neutrons at Mercury (Lawrence et al. 2017).

Second, if we assume Fig. 6 represents a map of <A>*, we can ask what element (or elements) might be the dominant contributor to <A>* variability (or Δ<A>*), as was done for <A> values on the Moon, Mercury, and Vesta (Lawrence et al. 2017). Lunar and vestan <A> analyses were constrained by the extensive chemical data that exist for Apollo, lunar meteorite, and HEDs. While there are no known meteorites from Ceres, Ceres's composition is most similar to the primitive (volatile-rich) CM and CI carbonaceous chondrites (McSween et al. 2017; Prettyman et al. 2017). Therefore, as a starting point, we have determined the elemental contributions and variations to <A>* for 20 different CM and CI meteorites from the meteoritic compositional database given by Nittler et al. (2004) (Fig. 7). The three largest contributors to <A>* are O, Fe, and Si. In terms of the range of elemental abundance, Fe also shows significant variability for the different CI and CM meteorites, being twice that of either Mg or S. Petrologically, variability in bulk Fe, Mg, and S in the CM and CI meteorites is largely due to variations in metal/sulfide abundance and mafic mineral composition, which are two diagnostic properties separating chondritic meteorite groups (Brearley and Jones 1998). Bulk Fe and S are affected by the metal/sulfides, while bulk Fe and Mg are influenced by the mafic minerals, and/or Fe-oxides (e.g., magnetite) and Fe/Mg phyllosilicates resulting from aqueous alteration of metals and primary silicates, respectively. Since bulk Fe is affected by both petrologic properties, and its proportion to other

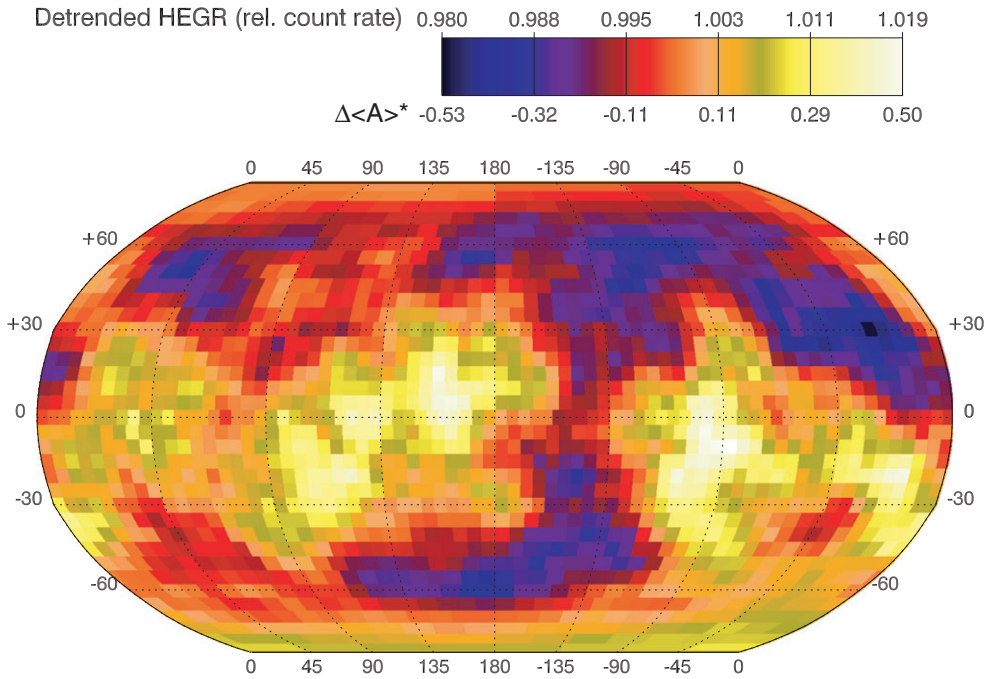

Fig. 6. Map of detrended HEGR values across Ceres's surface. The top numbers on the scale bar show relative count rate; the bottom numbers show variations in water-free average atomic mass (Δ < A > *) from the mean value. (Color figure can be viewed at wileyonlinelibrary.com.)

elements more or less held constant with subsequent aqueous alteration, it is understandable why Fe shows the largest range of all elements in Fig. 7. This suggests that for Ceres-like compositions (and possibly Ceres itself) Δ<A>* is driven by variations in Fe abundances.

This same analysis has been carried out for the five Ceres-like compositions given by Prettyman et al. (2017). These include carbonaceous chondrites (CC) and three extrapolated compositions (E) with lower Fe concentrations between that of CC and Halley's dust (HD). As with the carbonaceous chondrite compositions discussed above, the largest contributors to <A>* from these five materials are O, Fe, and Si (Fig. 8); however, the elements driving the largest variability are S and Fe. We note that the three artificial compositions derived by Prettyman et al. (2017) (E1, E2, and E3) have S values that fall outside the range spanned by CCs and Halley's dust (E >> CC = HD). Nevertheless, even for this set of compositions, Fe is a major contributor to <A>* variability. In summary, based on these element variation analyses, the dominant contributor to Δ<A>* is likely Fe. If Fe abundances can be measured independently with GRaND gamma ray data, then the Fe contribution to Δ<A>* could be removed and any remaining residual might be related to other element variations, such as Mg or S.

Given that Fe appears to be the dominant source of <A>* variations, what does this imply about <A>* and Fe variations across Ceres? Based on the WEH-detrended model values (Fig. 2b), WEH-free HEGRs change by roughly 4% per atomic mass unit (amu). Using the correlation of Fig. 2b, the relative WEH-free HEGR variations can be cast as Δ<A>*. This Δ<A>* scale is shown in Fig. 6 and has a variation across Ceres of ±0.5 amu. Since we do not have a complete set of average elemental abundances for Ceres from which to derive absolute <A>* values across Ceres's surface, this scale is necessarily relative. If Δ<A>* is attributed entirely to Fe variations, then this translates into a ±2.5 wt% variation in Fe abundances.

Prettyman et al. (2017) reported a mean Fe value for Ceres's surface of 16±1 wt%. On a plot of Fe versus WEH, this value lies below the expected water dilution trend for CM and CI chondrites, indicating that Ceres's nonhydrous composition is depleted in Fe relative to the CM and CI chondrites. Our HEGR-inferred Fe variations (±2.5 wt%) can be combined with the Prettyman et al. (2017) mean to yield a full allowed range of 16±3.5 wt% Fe. For the average equatorial Fe and WEH abundances given by Prettyman et al. (2017), this variation would result in the maximum allowed Fe abundances reaching up to the CI chondrite water dilution trend given by Prettyman et al. (2017) (Fig. 9). These highest <A>* locations on Ceres may be consistent with CI compositions. This result indicates that regions with the

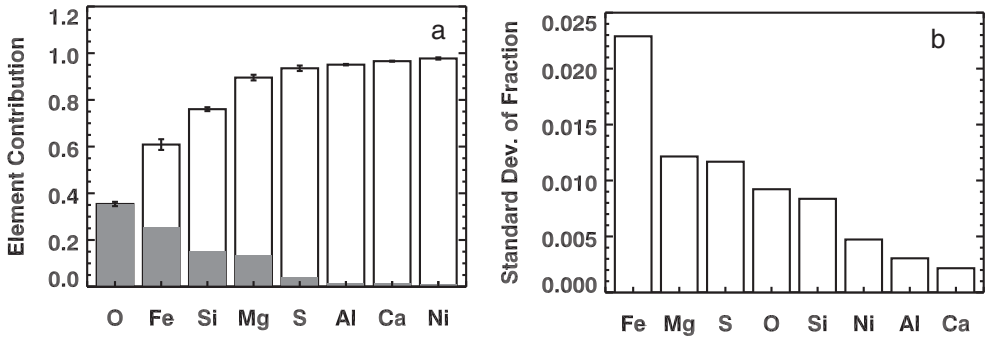

Fig. 7. a) Cumulative (white bars) and fractional (gray bars) contributions to <A>* for CM and CI meteorite compositions from the Nittler et al. (2004) database. The error bars denote the range of elemental variability across the samples. b) Elemental variations (taken from the error bars in [a]) sorted by most to least variability.

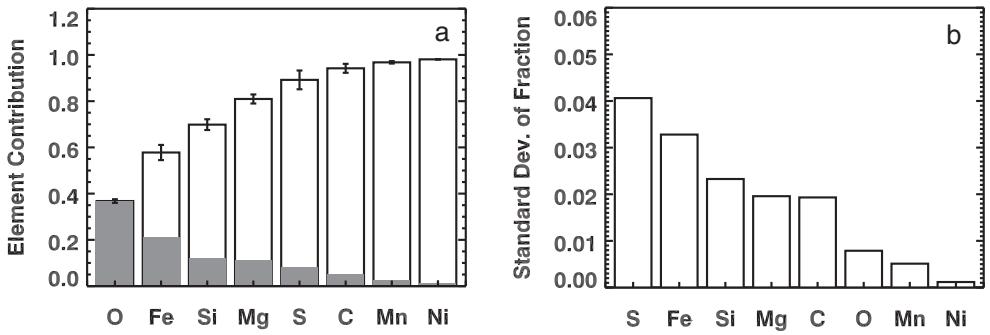

Fig. 8. a) Cumulative (white bars) and fractional (gray bars) contributions to <A>* for the average CM and CI meteorite compositions along with the E1, E2, and E3 compositions, all from Prettyman et al. (2017). The error bars denote the range of elemental variability across the five soils. b) Elemental variations (taken from the error bars in [a]) sorted by most to least variability.

highest <A>* values on Ceres may be similar to the composition of CI chondrites. Conversely, the regions with the lowest <A>* values are likely least similar to the composition of CI chondrites.

COMPARISON OF HEGR AND OTHER DAWN DATA SETS

To gain a better understanding of what the HEGR data reveal about Ceres, here we compare the HEGR map with other global information derived from Dawn data, namely a map of crater density, a global geologic map, and reflectance band-depth data (2.7 and 3.1 μm) from Dawn's Visible and Infrared (VIR) spectrometer (Fig. 10).

Crater density information is derived from the crater catalog given by Hiesinger et al. (2016) for craters >20 km in size. Specifically, a crater density map (Fig. 10a) was created using the method of kernel density estimation (Rosenblatt 1956; Parzen 1962) with Gaussian kernels, chosen for smoothness. Using a fourfold cross-validation technique (Rudemo 1982), the optimal bandwidth was found to be 0.24 radians, or 114 km. The general features of the crater density map are similar to the color-coded crater density map of Hiesinger et al. (2016), where it was concluded that the locations of low crater densities were likely due to impact-driven resurfacing from large craters such as Kerwan (11°S, 123°E), Yalode (42°S, 290°E), and Urvara (46°S, 249°E) as well as large basins (Planitiae like Vendimia Planitia) (Marchi et al. 2016). In addition to the crater density color scale, Fig. 10a also shows two broad contours that outline the highest (white) and lowest (black) crater density regions across Ceres. The contours were chosen to delineate the lowest, middle, and top third of the crater-density cumulative distribution.

The global geologic map (Fig. 10b) is taken from Mest et al. (2017), and is an updated map of that first published by Buczkowski et al. (2016). This map was generated using image, spectral, and topographic data from Dawn's High-Altitude Mapping Orbit (HAMO). In a broad context, this map defines several geologic units. Cratered terrains (the outside portion of the black contours in Fig. 10b) represent the oldest materials on Ceres, and are dominantly in the equatorial and northern portions of Ceres. Smooth terrains and units of the Urvara/Yalode system are broadly related to the

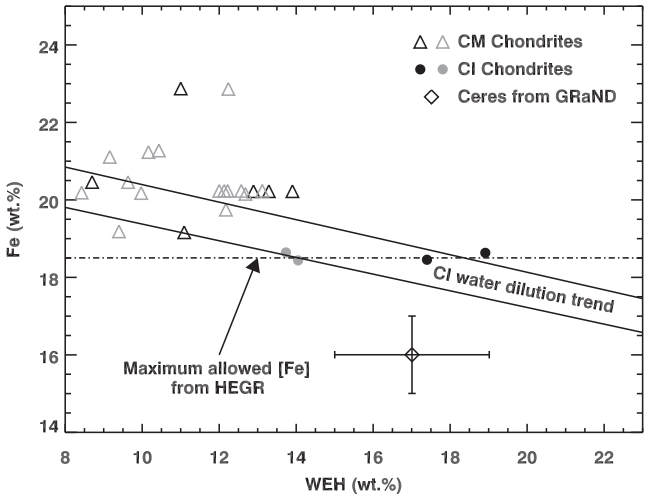

Fig. 9. Data from fig. 4 of Prettyman et al. (2017), where the horizontal dashed line represents the maximum Fe abundance allowed by the HEGR measurements as described in the text. Black triangles and circles show hydrogen measured via mass spectrometry and gray triangles and circles show hydrogen measured via thermogravimetric analysis as described by Prettyman et al. (2017). Water dilution trends, in which Fe concentration is adjusted by adding or removing water, are displayed for the CI chondrites. Ceres's equatorial average is shown as a point with error bars indicating total uncertainty of the equatorial average.

large impact craters Kerwan, Urvara, and Yalode. The white contours in Fig. 10b (also labeled "Restricted ejecta" in Fig. 12b) delineate geologic boundaries of large crater units most closely associated with detrended HEGR enhancements. A legend of the detailed map units is given in Mest et al. (2017).

Reflectance band-depth measurements from Dawn's VIR spectrometer were taken from Ammannito et al. (2016). Specifically, maps of 2.7 and 3.1 μm band depths represent abundance variations of phyllosilicates where the 2.7 μm band indicates Mg-OH phyllosilicate, such as serpentine, and the 3.1 μm band indicates ammoniated phyllosilicate (De Sanctis et al. 2015). Given the lack of variation in band center location, the composition of those phases (i.e., abundance of Fe to Mg in the mineral structure) appears to be consistent across the surface (Ammannito et al. 2016). Because the VIR data have significantly higher spatial resolution than the GRaND data, we have smoothed the VIR data using a large-area footprint to better represent the GRaND data (Figs. 10c and 10d). As with the crater-density map, contours based on the high, medium, and low band depth cumulative distributions are shown in Figs. 10c and 10d.

Figure 11 shows the detrended HEGR map (proportional to <A>*) with the contours of Fig. 10 superimposed. For reference, outlines of five large craters (Kerwan, Dantu, Urvara, Yalode, and Occator) are shown in Figs. 11a and 11b. Figure 12 shows histograms of the HEGR values separated by the different contours for each of the crater density, geologic, and band-depth maps. Figure 11a shows that the high HEGR values around the large western craters (Urvara and Yalode) correspond to locations of lower crater density. For the eastern craters, the relationship between crater density and HEGR values is less clear, but high HEGR values are nevertheless located in regions with low crater density. In contrast, locations with high crater densities tend to show lower HEGR values, although this is not uniformly the case across all of Ceres's surface. The relationship between crater density and HEGR values described above is also illustrated in Figure 12a, where the HEGR histogram for low–crater-density regions is shifted to high HEGR values, and the HEGR histogram for high–crater-density regions has a centroid at relatively low HEGR values.

The comparison of geologic units and HEGR values shows that the older cratered terrains tend to have lower HEGR values, and units associated with the large craters have higher HEGR values. When the crater units are restricted to locations closer to the large craters Dantu, Kerwan, Urvara, and Yalode (white contours in Figs. 10b and 11b), there is a more separated enhancement of high HEGR values (orange histogram in Fig. 12b) from lower HEGR values in cratered terrains.

The comparison of VIR band depth data with HEGR values generally shows that locations with higher abundances of Mg-OH and NH_4-bearing phyllosilicates (greater band depth) tend to have higher HEGR values. We note that the medium and low 3.1 μm band depth data (ammoniated phyllosilicate) both show similar low HEGR values, whereas the 2.7 μm band depth data (Mg-OH phyllosilicate) have a more monotonic relationship of low-to-high band depths corresponding to low-to-high HEGR values. The somewhat stronger correlation with the 2.7 μm band depth suggests that the concentration of Fe-bearing minerals increases with the concentration of Mg phyllosilicates. Ceres's surface has experienced a high degree of aqueous alteration (e.g., Ammannito et al. 2016). Iron replaces Mg in serpentine as alteration progresses, producing magnetite and/or iron sulfide (e.g., McSween et al. 2017). On Ceres, iron is probably found in these mineral phases. Thus, regions with higher <A>* may contain higher concentrations of magnetite. In a homogeneous, closed system, the observed correlation is not expected, which supports the idea that materials on Ceres's surface experienced chemical fractionation. Furthermore, these data may be useful in constraining the ammoniated phyllosilicate phase hypothesized to be causing the 3.1 μm feature.

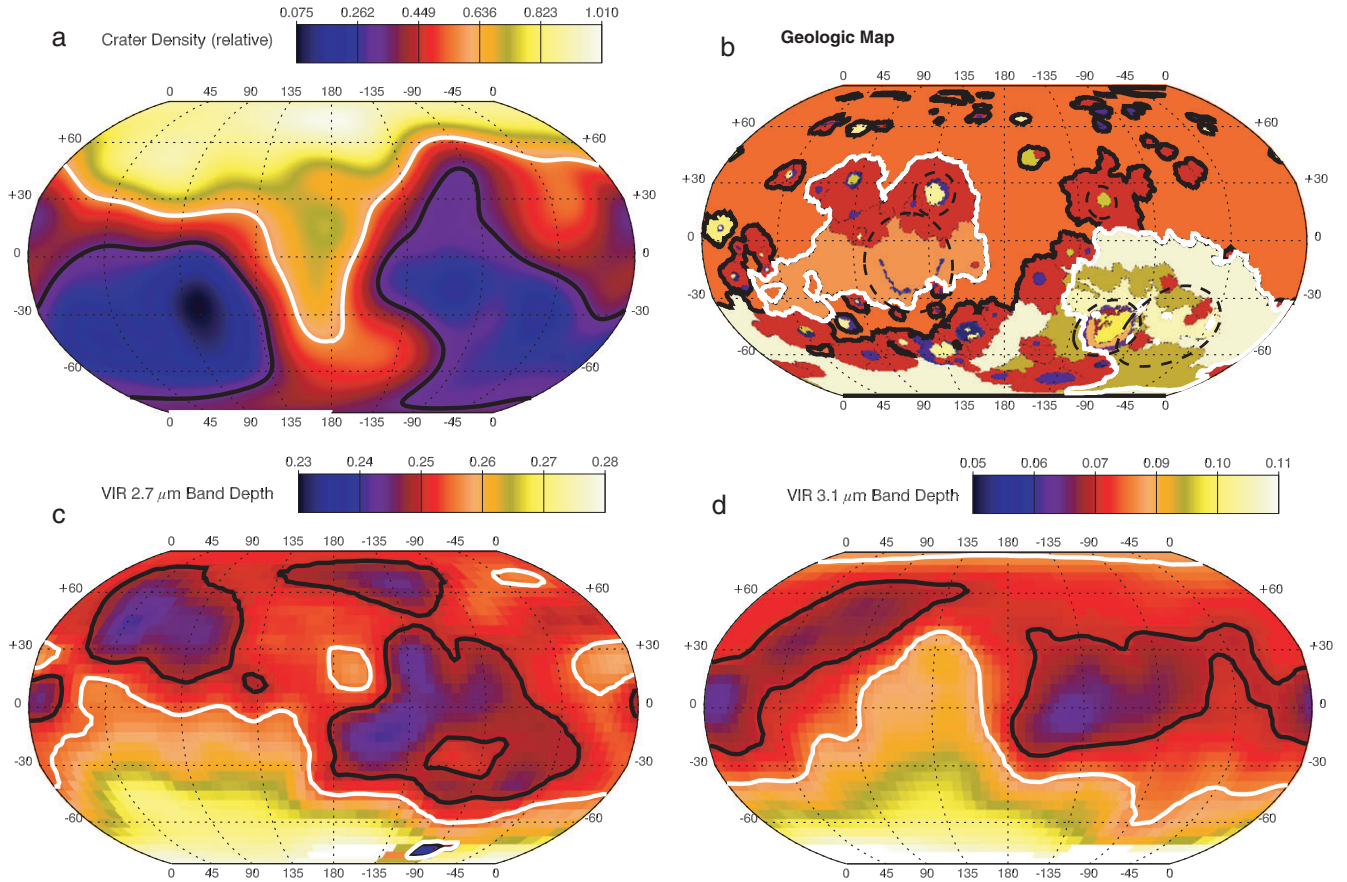

Fig. 10. a) Global map of Ceres's relative crater density as derived from the crater catalog of Hiesinger et al. (2016), where the values shown are relative to the maximum value. The contours represent boundaries between high and low values of crater densities. b) Geologic map from Mest et al. (2017), where the black contour delineates the boundary for the crater terrain unit; the white contour delineates the boundary for the restricted large-crater ejecta terrains as described in the text. c) Smoothed map of VIR spectrometer band depths for 2.7 μm. The white and black contours represent boundaries between high and low band depths, respectively. d) Smoothed map of VIR spectrometer band depths for 3.1 μm. The white and black contours represent boundaries between high and low band depths, respectively. The original VIR band depth data are taken from Ammannito et al. (2016). (Color figure can be viewed at wileyonlinelibrary.com.)

De Sanctis et al. (2015) proposed two options: annite, which has 33 wt% Fe, and montmorillonite, which has <1 wt% Fe. Given the lack of strong correlation between the 3.1 μm feature and <A>*, annite seems like the less likely of the two options. When the spectral library of ammoniated phyllosilicates gets expanded, alternatives may be proposed in the future. Our <A>* findings may be useful in testing those hypotheses (i.e., ruling out exceptionally Fe-rich phases).

In summary, these comparisons point to the following ideas. First, the detrended HEGR map provides evidence that Ceres has nonhydrogen compositional differences between older, more highly cratered terrains and younger terrains that are broadly related to the ejecta of the largest craters. Specifically, the younger, ejecta-like terrains tend to have higher <A>* values. Furthermore, if the systematic elemental relationships of CM/CI meteorites hold for Ceres materials, then these higher <A>* values would imply these locations are systematically elevated in Fe concentrations. Second, the comparison of VIR and HEGR data provide evidence that locations of enhanced Mg-OH phyllosilicates also have higher <A>* values, and possibly higher Fe abundances.

DISCUSSION AND SUMMARY

In this study, we have presented a map of HEGRs measured by GRaND from Dawn's LAMO phase about Ceres. Both the data and models of HEGR production show that for Ceres-like compositions, the primary variation of HEGRs across Ceres's surface is due to hydrogen variations. However, HEGR production models show that hydrogen variations can be decoupled

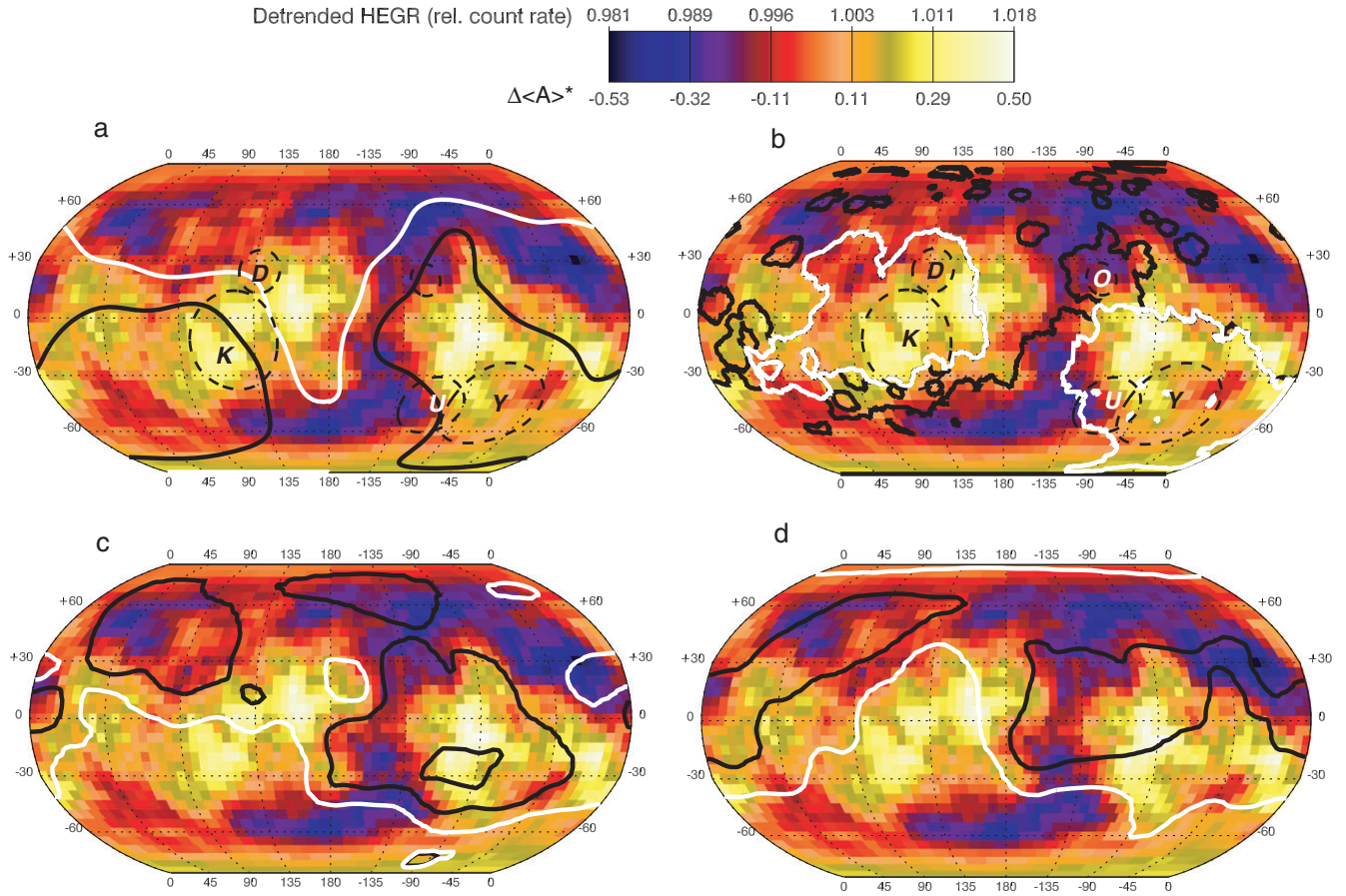

Fig. 11. Detrended HEGR data with overlain contours for (a) crater densities; (b) geologic map boundaries; (c) 2.7 μm VIR band depths; (d) 3.1 μm VIR band depths. Outlines of six large craters are indicated by dashed circles in (a) and (b), and are labeled as following: K = Kerwan (11°S, 123°E); D = Dantu (24°N, 137°E); U = Urvara (46°S, 249°E); Y = Yalode 42°S, 290°E); O = Occator (20°N, 239°E). (Color figure can be viewed at wileyonlinelibrary.com.)

from nonhydrogen variations and the remaining variations correspond to a water-free average atomic mass that we denote as <A>*. When this detrending is carried out on the measured HEGR data, the resulting map shows variations that indicate nonhydrogen composition variations on Ceres's surface. To the extent that the detrended HEGR map represents Δ<A>*, the data reveal that <A>* varies by ±0.5 amu across Ceres's surface. Analyses of CM/CI meteorites, the closest compositional analog to Ceres's surface, show that variations in Fe are likely the dominant source of variations in <A>*. Regions with the highest <A>* may preserve the primitive chondritic composition that accreted to form Ceres and others may have fractionated from this composition via various processes.

When the HEGR map is compared to other Dawn data, we find that locations with higher <A>* values (and possibly higher Fe concentrations) tend to be located in younger, less cratered terrains that are associated with impact ejecta of Ceres's largest craters. In some instances, these locations of higher <A>* values are also associated with higher abundances of Mg-OH phyllosilicates and NH_4. Conversely, locations with lower <A>* values (and possibly lower Fe concentrations) are found in older, more heavily cratered terrains.

A possible reason for this variability is overturn of the surface by large impacts. If Ceres hosted a global ocean early in its history (e.g., Castillo-Rogez and Young 2016), then it is likely that Fe-rich particles such as magnetite or iron sulfide could sink faster than silicate-rich particles (e.g., Scott et al. 2002), consistent with the idea proposed by Prettyman et al. (2017) for the observed depletion of iron in Ceres's regolith. This implies that iron might be concentrated at depth and that iron-rich material could be exposed by large impacts.

Additional insight into the HEGR map can be gained through two other avenues. First, the spatial association of mapped HEGR variations can in principle be improved by using spatial reconstruction algorithms on the GRaND data, as has been done for

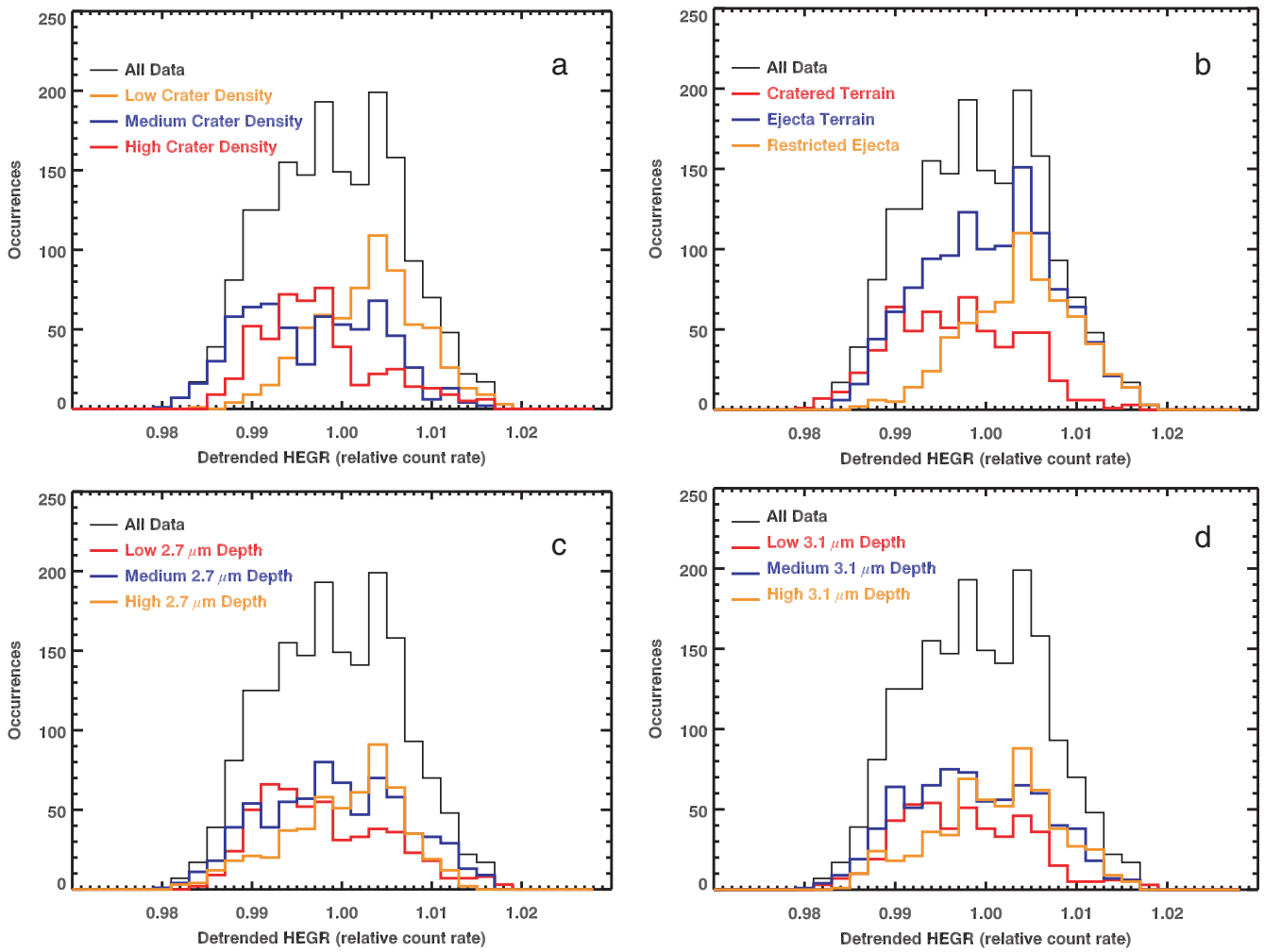

Fig. 12. Histograms of detrended HEGR data, where the HEGR data are binned based on the contours of (a) crater densities; (b) geologic map boundaries; (c) 2.7 μm VIR band depths; (d) 3.1 μm VIR band depths. (Color figure can be viewed at wile yonlinelibrary.com.)

similar nuclear spectroscopy data on other planetary bodies (e.g., Lawrence et al. 2007; Wilson et al. 2018). Finally, if the Dawn mission pursues its plan to carry out lower altitude GRaND measurements than were done for the LAMO mission phase, such measurements could improve the GRaND intrinsic spatial resolution by up to a factor of two, thus further refining the identified spatial relationships between HEGR data and other Dawn measurements in at least a few regions.

Acknowledgments—The Dawn mission is led by the University of California, Los Angeles, and managed by the Jet Propulsion Laboratory, Pasadena, California under the auspices of the NASA Discovery Program Office. Support for this work was provided by the Dawn mission program. Part of this work was supported by grant ASI-INAF I/004/12/1. The authors thank Larry Nittler and Insoo Jun for a very conscientious job of reviewing the manuscript. W. Feldman also thanks Los Alamos National Laboratory for providing an office and access to their library during the summer months that he was working on this project. GRaND is operated by the Planetary Science Institute under contract with JPL. Science Reduced Data Records and housekeeping data acquired by GRaND during its Ceres encounter and used in this study are available from NASA's Planetary Data System (https://pdssbn.astro.umd.edu/data_sb/missions/dawn/index.shtml). The authors have no conflict of interest to declare.

Editorial Handling—Dr. Harry McSween

REFERENCES

Ammannito E., DeSanctis M. C., Ciarniello M., Frigeri A., Carrozzo F. G., Combe J. P., Ehlmann B. L., Marchi S.,

McSween H. Y., Raponi A., Toplis M. J., Tosi F., Castillo-Rogez J. C., Capaccioni F., Capria M. T., Fonte S., Giardino M., Jaumann R., Longobardo A., Joy S. P., Magni G., McCord T. B., McFadden L. A., Palomba E., Pieters C. M., Polanskey C. A., Rayman M. D., Raymond C. A., Schenk P. M., Zambon F., and Russell C. T. 2016. Distribution of phyllosilicates on the surface of Ceres. *Science* 353. https://doi.org/10.1126/science.aaf4279.

Beck A. W., Lawrence D. J., Peplowski P. N., Prettyman T. H., McCoy T. J., McSween H. Y. Jr., Toplis M. J., and Yamashita N. 2015. Using HED meteorites to interpret neutron and gamma-ray data from asteroid 4 Vesta. *Meteoritics & Planetary Science* 50:1311–1337. https://doi.org/10.1111/maps.12467.

Beck A. W., Lawrence D. J., Peplowski P. N., Viviano-Beck C. E., Prettyman T. H., McCoy T. J., McSween H. Y. Jr., and Yamashita N. 2017. Igneous lithologies on asteroid (4) Vesta mapped using gamma ray and neutron data. *Icarus* 286:35–45. https://doi.org/10.1016/j.icarus.2017.01.008.

Brearley A. J. and Jones R. H. 1998. Chondritic meteorites. In *Planetary materials*, edited by Papike J. J. Reviews in Mineralogy, vol. 36. Washington, D.C.: Mineralogical Society of America. pp. 3-001–3-398.

Buczkowski D. L., Schmidt B. E., Williams D. A., Mest S. C., Scully J. E. C., Ermakov A. I., Preusker F., Schenk P., Otto K. A., Hiesinger H., O'Brien D., Marchi S., Sizemore H., Hughson K., Chilton H., Bland M., Byrne S., Schorghofer N., Platz T., Jaumann R., Roatsch T., Sykes M. V., Nathues A., De Sanctis M. C., Raymond C. A., and Russell C. T. 2016. The geomorphology of Ceres. *Science* 353. https://doi.org/10.1126/science.aaf4332.

Castillo-Rogez J. C. and Young E. D. 2016. Origin and evolution of volatile-rich planetesimals. In *Planetesimal differentiation*, edited by Elkins-Tanton L. and Weiss B. Cambridge: Cambridge University Press.

Cochran D. R. F., Dean P. N., Gram P. A. M., Knapp E. A., Martin E. R., Nagle D. E., Perkins R. B., Shlaer W. J., Thiessen H. A., and Theriot E. D. 1972. Production of charged pions by 730-Mev protons from hydrogen and selected nuclei. *Physical Review D* 6:3085. https://doi.org/10.1103/PhysRevD.6.3085.

Combe J. P., McCord T. B., Tosi F., Ammannito E., Carrozzo F. G., De Sanctis M. C., Raponi A., Byrne S., Landis M. E., Hughson K. H. G., Raymond C. A., and Russell C. T. 2016. Detection of local H_2O exposed at the surface of Ceres. *Science* 353. https://doi.org/10.1126/science.aaf3010.

De Sanctis M. C., Ammannito E., Raponi A., Marchi S., McCord T. B., McSween H. Y., Capaccioni F., Capria M. T., Carrozzo F. G., Ciarniello M., Longobardo A., Tosi F., Fonte S., Formisano M., Frigeri A., Giardino M., Magni G., Palomba E., Turrini D., Zambon F., Combe J.-P., Feldman W., Jaumann R., McFadden L. A., Pieters C. M., Prettyman T., Toplis M., Raymond C. A., and Russell C. T. 2015. Ammoniated phyllosilicates with a likely outer solar system origin on (1) Ceres. *Nature* 528:241–244. https://doi.org/10.1038/nature16172.

De Sanctis M. C., Raponi A., Ammannito E., Ciarniello M., Toplis M. J., McSween H. Y., Castillo-Rogez J. C., Ehlmann B. L., Carrozzo F. G., Marchi S., Tosi F., Zambon F., Capaccioni F., Capria M. T., Fonte S., Formisano M., Frigeri A., Giardino M., Longobardo A., Magni G., Palomba E., McFadden L. A., Pieters C. M., Jaumann R., Schenk P., Mugnuolo R., Raymond C. A., and Russell C. T. 2016. Bright carbonate deposits as evidence of aqueous alteration on (1) Ceres. *Nature* 536:54–57. https://doi.org/10.1038/nature18290.

Feldman W. C., Pathare A., Maurice S., Prettyman T. H., Lawrence D. J., Milliken R. E., and Travis B. J. 2011. Mars Odyssey neutron data: 2. Search for buried excess water ice deposits at non-polar latitudes on Mars. *Journal of Geophysical Research* 116:E11009. https://doi.org/10.1029/2011JE003806.

Hiesinger H., Marchi S., Schmedemann N., Schenk P., Pasckert J. H., Neesemann A., O'Brien D. P., Kneissl T., Ermakov A. I., Fu R. R., Bland M. T., Nathues A., Platz T., Williams D. A., Jaumann R., Castillo-Rogez J. C., Ruesch O., Schmidt B., Park R. S., Preusker F., Buczkowski D. L., Russell C. T., and Raymond C. A. 2016. Cratering on Ceres: Implications for its crust and evolution. *Science* 353. https://doi.org/10.1126/science.aaf4759.

Lawrence D. J., Puetter R. C., Elphic R. C., Feldman W. C., Hagerty J. J., Prettyman T. H., and Spudis P. D. 2007. Global spatial deconvolution of Lunar Prospector Th abundances. *Geophysical Research Letters* 34:L03201–L03201. https://doi.org/10.1029/2006GL028530.

Lawrence D. J., Peplowski P. N., Prettyman T. H., Feldman W. C., Bazell D., Mittlefehldt D. W., Reedy R. C., and Yamashita N. 2013. Constraints on Vesta's elemental composition: Fast neutron measurements by Dawn's gamma ray and neutron detector. *Meteoritics & Planetary Science* 48:2271–2288. https://doi.org/10.1111/maps.12187.

Lawrence D. J., Peplowski P. N., Plescia J. B., Greenhagen B. T., Maurice S., and Prettyman T. H. 2015. Bulk hydrogen abundances in the lunar highlands: Measurements from orbital neutron data. *Icarus* 255:127–134. https://doi.org/10.1016/j.icarus.2015.01.005.

Lawrence D. J., Peplowski P. N., Beck A. W., Feldman W. C., Frank E. A., McCoy T. J., Nittler L. R., and Solomon S. C. 2017. Compositional terranes on Mercury: Information from fast neutrons. *Icarus* 281:32–45. https://doi.org/10.1016/j.icarus.2016.07.018.

Marchi S., Ermakov A. I., Raymond C. A., Fu R. R., O'Brien D. P., Bland M. T., Ammannito E., De Sanctis M. C., Bowling T., Schenk P., Scully J. E. C., Buczkowski D. L., Williams D. A., Hiesinger H., and Russell C. T. 2016. The missing large impact craters on Ceres. *Nature Communications* 7:12257. https://doi.org/10.1038/ncomms12257.

Maurice S., Feldman W., Diez B., Gasnault O., Lawrence D. J., Pathare A., and Prettyman T. 2011. Mars Odyssey neutron data: 1. Data processing and models of water-equivalent-hydrogen distribution. *Journal of Geophysical Research* 116:E11008. https://doi.org/10.1029/2011JE003810.

McSween H. Y., Emery J. J. P., Rivkin A. S., Toplis M. J., Castillo-Rogez J. C., Prettyman T. H., De Sanctis M. C., Pieters C. M., Raymond C. A., and Russell C. T. 2017. Carbonaceous chondrites as analogs for the composition and alteration of Ceres. *Meteoritics & Planetary Science*. https://doi.org/10.1111/maps.12947.

Mest S. C., Crown D., Aileen Yingst R., Berman D., Williams D., Buczkowski D., Scully J., Platz T., Jaumann R., Roatsch T., Preusker F., Nathues A., Hiesinger H., Hendrik Pasckert J., Raymond C., and Russell C. 2017. The HAMO-based global geologic map of Ceres (abstract #7105). 3rd Planetary Data Workshop.

Nittler L. R., McCoy T. J., Clark P. E., Murphy M. E., Trombka J. I., and Jarosewich E. 2004. Bulk element

compositions of meteorites: A guide for interpreting remote-sensing geochemical measurements of planets and asteroids. *Antarctic Meteorite Research* 17:231–251.
Parzen E. 1962. Estimation of a probability density-function and mode. *Annals of Mathematical Statistics* 33:1065–1076. https://doi.org/10.1214/aoms/1177704472.
Pelowitz D. B. 2005. MCNPX User's Manual, Version 2.5.0. Los Alamos, New Mexico. 473 p.
Peplowski P. N. and Lawrence D. J. 2013. New insights into the global composition of the lunar surface from high-energy gamma rays measured by Lunar Prospector. *Journal of Geophysical Research-Planets* 118:671–688. https://doi.org/10.1002/jgre.20063.
Peplowski P. N., Lawrence D. J., Prettyman T. H., Yamashita N., Bazell D., Feldman W. C., Le Corre L., McCoy T. J., Reddy V., Reedy R. C., Russell C. T., and Toplis M. J. 2013. Compositional variability on the surface of 4 Vesta revealed through GRaND measurements of high-energy gamma rays. *Meteoritics & Planetary Science* 48:2252–2270. https://doi.org/10.1111/maps.12176.
Peplowski P. N., Bazell D., Evans L. G., Goldsten J. O., Lawrence D. J., and Nittler L. R. 2015. Hydrogen and major element concentrations on 433 Eros: Evidence for an L- or LL-chondrite-like surface composition. *Meteoritics & Planetary Science* 50:353–367. https://doi.org/10.1111/maps.12434.
Prettyman T. H. 2014. Remote sensing of chemical elements using nuclear spectroscopy. In *Encyclopedia of the solar system*, edited by Spohn T., Breuer D., and Johnson T. V. Amsterdam: Elsevier. pp. 1161–1183. ISBN: 978012415 8450
Prettyman T. H. 2016. Dawn GRaND Raw (EDR) Ceres Counts V1.0, Dawn-A-GRaND-2-EDR-Ceres-Counts-V1.0. NASA Planetary Data System.
Prettyman T. H. and Yamashita N. 2016. Dawn GRaND Calibrated (RDR) Ceres Counts V1.0, Dawn-A-GRaND-3-RDR-Ceres-Counts-V1.0. NASA Planetary Data System.
Prettyman T. H., Hagerty J. J., Elphic R. C., Feldman W. C., Lawrence D. J., McKinney G. W., and Vaniman D. T. 2006. Elemental composition of the lunar surface: Analysis of gamma ray spectroscopy data from Lunar Prospector. *Journal of Geophysical Research* 111:E12007–E12007. https://doi.org/10.1029/2005JE002656.
Prettyman T. H., Mittlefehldt D. W., Yamashita N., Lawrence D. J., Beck A. W., Feldman W. C., McCoy T. J., McSween H. Y., Toplis M. J., Titus T. N., Tricarico P., Reedy R. C., Hendricks J. S., Forni O., Le Corre L., Li J.-Y., Mizzon H., Reddy V., Raymond C. A., and Russell C. T. 2012. Elemental mapping by Dawn reveals exogenic H in Vesta's regolith. *Science* 338:242–246. https://doi.org/10.1126/science.1225354.
Prettyman T. H., Mittlefehldt D. W., Yamashita N., Beck A. W., Feldman W. C., Hendricks J. S., Lawrence D. J., McCoy T. J., McSween H. Y., Peplowski P. N., Reddy R. C., Toplis M. J., Le Corre L., Mizzon H., Reddy V., Titus T. N., Raymond C. A., and Russell C. T. 2013. Neutron absorption constraints on the composition of 4 Vesta. *Meteoritics & Planetary Science* 48:2211–2236. https://doi.org/10.1111/maps.12244.
Prettyman T. H., Yamashita N., Toplis M. J., McSween H. Y., Schörghofer N., Marchi S., Feldman W. C., Castillo-Rogez J., Forni O., Lawrence D. J., Ammannito E., Ehlmann B. L., Sizemore H. G., Joy S. P., Polanskey C. A., Rayman M. D., Raymond C. A., and Russell C. T. 2017. Extensive water ice within Ceres' aqueously altered regolith: Evidence from nuclear spectroscopy. *Science* 355:55–58. https://doi.org/10.1126/science.aah6765.
Rosenblatt M. 1956. Remarks on some nonparametric estimates of a density-function. *Annals of Mathematical Statistics* 27:832–837. https://doi.org/10.1214/aoms/1177728190.
Rudemo M. 1982. Empirical choice of histograms and kernel density estimators. *Scandinavian Journal of Statistics* 9:65–78.
Russell C. T., Raymond C. A., Ammannito E., Buczkowski D. L., De Sanctis M. C., Hiesinger H., Jaumann R., Konopliv A. S., McSween H. Y., Nathues A., Park R. S., Pieters C. M., Prettyman T. H., McCord T. B., McFadden L. A., Mottola S., Zuber M. T., Joy S. P., Polanskey C., Rayman M. D., Castillo-Rogez J. C., Chi P. J., Combe J. P., Ermakov A., Fu R. R., Hoffmann M., Jia Y. D., King S. D., Lawrence D. J., Li J.-Y., Marchi S., Preusker F., Roatsch T., Ruesch O., Schenk P., Villarreal M. N., and Yamashita N. 2016. Dawn arrives at Ceres: Exploration of a small, volatile-rich world. *Science* 353:1008–1010. https://doi.org/10.1126/science.aaf4219.
Scott H. P., Williams Q., and Ryerson F. J. 2002. Experimental constraints on the chemical evolution of large icy satellites. *Earth and Planetary Science Letters* 203:399–412.
Wilson J. T., Eke V. R., Massey R. J., Elphic R. C., Feldman W. C., Mauric S., and Teodoroe L. F. A. 2018. Equatorial locations of water on Mars: Improved resolution maps based on Mars Odyssey Neutron Spectrometer data. *Icarus* 299:148–160. https://doi.org/10.1016/j.icarus.2017.07.028.

APPENDIX: ANALYSIS OF GRAND HEGR DATA AT CERES

The processing steps used to derive the final HEGR map are similar to those used in prior analyses of GRaND data carried out for Vesta (Lawrence et al. 2013; Peplowski et al. 2013) and Ceres (Prettyman et al. 2017). The specific data used in this analysis were the GRaND Level 1b data (Reduced Data Records) given by Prettyman and Yamashita (2016). The processing includes selections and corrections with the time-series data, as well as mapping and smoothing of the final corrected data. As mentioned in the main text mapping data were taken from the Dawn LAMO and extended LAMO phases, for dates ranging from December 16, 2015 to August 10, 2016. Background data were taken from times both before and after the LAMO phases, including from March 16, 2015 to July, 2015 and January 29, 2017 to July 7, 2017.

The Level 1b data set excluded solar active times during both the LAMO and background mission phases (Prettyman and Yamashita 2016). In this study, data selections for LAMO were made to ensure that GRaND pointed within $\pm 13°$ nadir angle. Within these angles, no

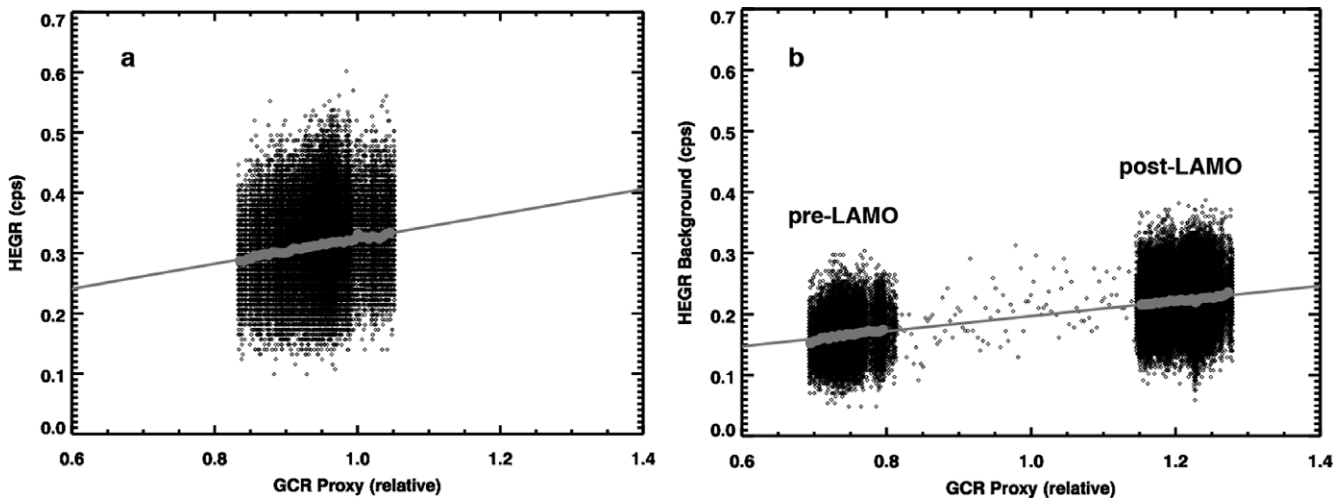

Fig. A1. a) HEGR count rate from the LAMO mission phases, in counts per second (cps), plotted as a function of the GCR proxy, which is the relative count rate from the GRaND triple-coincidence counter. b) HEGR count rate from the background mission phases plotted as a function of the GCR proxy. In both plots, the gray circles show binned count rates, and the solid line shows a linear fit to the binned count rate. Data from pre-LAMO and post-LAMO mission phases are labeled.

systematic biases were observed that were large enough to necessitate any corrections for viewing geometry. After final selections, the LAMO data set had 103,945 individual spectra with a total live-time data accumulation of 146 days. The total number of background spectra was 77,658 with a total live-time accumulation of 167 days.

Corrections for variations in galactic cosmic rays (GCR) were carried out in a manner similar to what was done for prior studies using the GRaND triple-coincidence counter, which is a proxy for GCR variations. Figure A1a shows the LAMO HEGR count rate plotted versus the normalized triple-coincidence count rate, or GCR proxy (black diamonds). The gray circles show binned values and the gray line shows a linear fit to the binned values. The HEGR data were detrended using the linear fit and normalized to the average count rate at the GCR proxy value of 1. The mean HEGR count rate is 0.324 counts per second (cps). Figure A1b shows background count rates versus the GCR proxy for both the pre- and post-LAMO background phases. The pre-LAMO background data have a GCR value <1, and post-LAMO data have a value greater than 1. There is a significant variation in background count rates across both background phases. Yet as seen, the binned count rate lines up very well across these phases. As with the LAMO data, the background data were detrended using the linear fit line, and normalized to the count rate at the GCR value of 1. The mean GCR-corrected background count rate is 0.197 cps. This background count rate was then subtracted from the total HEGR count rate. The mean net (background subtracted) HEGR count rate is 0.127 cps.

The background-subtracted HEGR count rate was corrected for solid-angle variations in a manner similar to prior studies using the solid-angle values given in the GRaND Level 1b data set. These final corrected count rates were mapped onto latitude/longitude pixels and smoothed using a two-dimensional Gaussian kernel that had a spatial width (sigma) of 0.9 Ceres radius. This is the map shown in Fig. 4.